
Anomaly Detection via Autoencoder Composite Features and NCE

Yalin Liao

Department of Electrical and Computer Engineering
 University of Delaware
 Newark, Delaware
 yalin@udel.edu

Austin J. Brockmeier

Department of Electrical and Computer Engineering
 Department of Computer and Information Sciences
 University of Delaware
 Newark, Delaware
 ajbrock@udel.edu

Abstract

Unsupervised anomaly detection is a challenging task. Autoencoders (AEs) or probabilistic models are often employed to model the data distribution of normal inputs and subsequently identify anomalous, out-of-distribution inputs by high reconstruction error or low likelihood. However, AEs may generalize to out-of-distribution inputs with similar features, causing detection failures when using reconstruction error alone as an anomaly score. We propose to enhance anomaly detection with AEs through joint density estimation over the AE’s latent features and reconstruction errors as a composite feature representation. Our approach uses a decoupled training approach: after training an AE to have a decorrelated latent space (or PCA on another pretrained network’s representation), noise contrastive estimation (NCE) is used to create the joint density function that serves as the anomaly score. We establish a principled motivation for this probabilistic modeling approach in terms of variational auto-encoders (VAE), specifically β -VAE. To further reduce the false negative rate we augment the NCE training by creating artificially lower reconstruction errors to ensure density decreases with higher errors and also adversarially optimize the contrastive Gaussian noise distribution. Experimental assessments on multiple benchmark datasets demonstrate that the proposed approach matches or exceeds the performance of state-of-the-art anomaly detection algorithms.

1 Introduction

The goal of anomaly detection is to identify observations that deviate from a given typical distribution [Chandola et al., 2009]. Along with the overall rise of deep learning, neural network-based anomaly detectors are often used for image distributions [Seeböck et al., 2016, Ruff et al., 2018, Sabokrou et al., 2018]. Autoencoders (AEs), often with convolutional architectures, are trained on the ‘normal’ data and widely applied for anomaly detection in one of two distinct cases. In the first case, the reconstruction error of an instance serves as the anomaly score [Sakurada and Yairi, 2014, Xia et al., 2015, Chen et al., 2018]. In the second case, the AE’s learned latent representation of the data in the bottleneck layer are treated as features, and subsequently, a machine learning or statistical approach

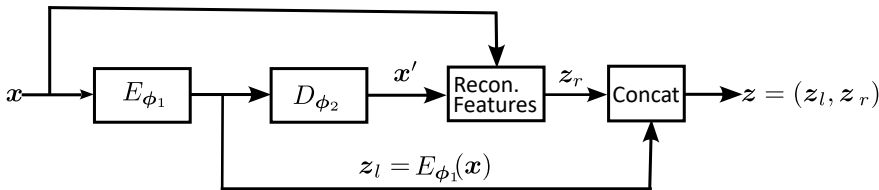
is employed to detect anomalies based on this learned representation [Andrews et al., 2016, Sabokrou et al., 2018, Xu et al., 2015].

In contrast to the prevailing majority of prior studies, which solely utilize either latent representation or reconstruction error as features, our approach incorporates both types of features for anomaly detection. A composite feature vector is formed by concatenating the latent representation at the bottleneck layer with reconstruction error metrics for the AE’s output as additional features. In particular, we train a constrained AE on normal images or use a pretrained neural network that embeds the images into a vector-space followed by PCA on the training set to provide the principal components and PCA reconstruction metrics. Finally, we use noise contrastive estimation (NCE) [Gutmann and Hyvärinen, 2010, 2012] to estimate a log-likelihood function in terms of this composite feature, which will serve as the anomaly score.

The composite feature enhances the performance of our method across a range of datasets, and we propose techniques to adjust the AE to be better suited for the subsequent NCE, which trains a network to distinguish the latent representation of typical input from Gaussian noise. Firstly, the architecture of the AE is designed such that first and second moments of the latent representation better match a standard Gaussian. Specifically, the batch normalization is introduced to ensure a zero-mean and unit-variance latent representation. Additionally, a covariance loss is introduced to encourage diagonal covariance, mitigating a singular covariance matrix. This will objectively encourage the development of statistically uncorrelated latent feature, making the composite feature better suited for NCE. These enhancements for a deterministic AE echo the goal of disentanglement and Gaussian prior in an β -VAE [Higgins et al., 2017].

We justify the modeling the joint distribution of the composite feature via NCE through an analysis of Latent Space Autoregression (LSA) [Abati et al., 2019] and β -VAE [Higgins et al., 2017], which seek to model the data likelihood. In particular, NCE avoids assuming an exponential-type likelihood for the reconstruction errors, allowing for heteroskedasticity. Additionally, we enhance the NCE through systematic data augmentation of the reconstruction features. We introduce additional normal instances with artificial reconstruction features when training the estimation network to ensure that the marginal density function for low reconstruction errors is no less than the noise distribution. This decreases the probability of predicting abnormal points as normal points. Overall, our proposed method uses an enhanced NCE on the composite feature while augmenting with artificial reconstruction features and we refer to the proposed method as Composite feature Augmented NCE (**CANCE**). Figure 1 overviews the proposed approach with the mathematical notation as in Section 3. Experimental results

Step 1. Train AE for the composite feature z



Step 2. Train NCE for anomaly detection

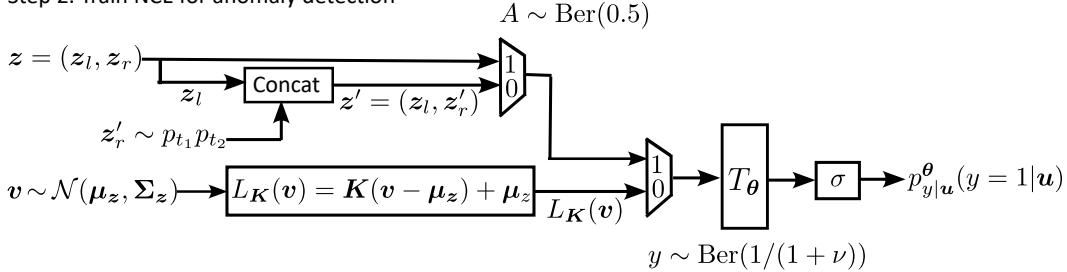


Figure 1: Proposed composite feature Augmented NCE (**CANCE**) for anomaly detection.

on multiple benchmark datasets demonstrate that the proposed approach matches the performance of prevalent state-of-the-art anomaly detection algorithms. An ablation study demonstrates the

contribution of the proposed additions to improve the anomaly detection performance. Finally, we demonstrate the generality of the two-step composite approach by substituting the AE with a pretrained network representation followed by PCA, where the principal components and the PCA reconstruction error form the composite features.

2 Related Work

Various strategies for anomaly detection are explored by approximating the density function of normal instances [Abati et al., 2019], such as Kernel Density Estimation (KDE) [Parzen, 1962] or parametric modeling such as Gaussian mixture model (GMM) [Bishop, 1994], where anomalies are identified by their low modeling probabilities. Although KDE and GMM perform reasonably well in low-dimensional scenarios, both suffer from the curse of dimensionality [Ruff et al., 2021]. Additionally, for image domains, directly applying modeling the density yields poor performance. Instead, density estimation or parametric modeling can be applied to the latent learning representations of AEs [Andrews et al., 2016, Sabokrou et al., 2018, Xu et al., 2015] as is common in prior work. This is supported by the fact that the true effective dimensionality is significantly smaller than the image dimensionality [Ruff et al., 2021]. Almost all prior work on using AE for anomaly detection have relied on either scores derived from latent features or from reconstruction error. One prior work, the Autoencoding Gaussian mixture model (DAGMM) [Zong et al., 2018], also integrates latent and reconstruction features for anomaly detection, wherein an AE and a GMM are jointly optimized for their parameters. Like DAGMM, we incorporate both latent features and reconstruction errors for anomaly detection. The key difference in our approach is that we adopt noise contrast estimation as non-parametric machine learning based approach for density estimation, which allows us to sidestep the challenges associated with forming a GMM, including specifying the number of mixture components in the DAGMM.

Alternatives to AEs include deep generative model techniques that enable modeling more complicated ‘normal’ data to enhance anomaly detection. While deep energy-based models [Zhai et al., 2016] have been used, their reliance on Markov chain Monte Carlo (MCMC) sampling creates computationally expensive training. Alternatively, autoregressive models [Salimans et al., 2017] and flow-based generative models [Kingma and Dhariwal, 2018] have been used to detect outliers via direct likelihood estimation. However, these approaches tend to assign high likelihood scores to anomalies as reported in recent literature [Choi et al., 2018, Ren et al., 2019, Yoon et al., 2024].

Variational Autoencoders (VAEs) can approximate the distribution of normal data via Monte Carlo sampling from the prior, thereby making them effective tools for anomaly detection. However, experiments in previous work [Nalismick et al., 2018, Xu et al., 2018] have demonstrated that utilizing the reconstruction probability [An and Cho, 2015] as an alternative can lead to improved performance.

Finally, Generative Adversarial Network (GAN) [Goodfellow et al., 2014] provide an implicit model of data distribution have been refined for application in anomaly detection [Di Mattia et al., 2019]. Most GAN-based approaches, such as AnoGAN [Schlegl et al., 2017] and EGBAD [Zenati et al., 2018], assume that after training the generator can produce normal points from the latent space better than anomalies, and naturally the discriminator, trained to distinguish between the generated data and the input data, could work as the anomaly measure. However, the optimization of GAN-based methods is challenged by convergence issues and mode collapse [Metz et al., 2016].

3 Proposed Method

We present a two-step methodology for anomaly detection. First, we employ a decoupled Autoencoder (AE) to construct a composite feature. Subsequently, we utilize a network trained with noise contrastive estimation (NCE) to estimate the negative log-likelihood function based on the composite feature, which serves as the scoring function, with higher values indicating anomalies and lower values signifying normality.

3.1 Method Introduction

For input data $\mathbf{x} \sim p_{d_0}$ in the data space \mathbb{R}^{d_0} distributed according to p_{d_0} , we propose to estimate an anomaly score function $S : \mathbb{R}^{d_0} \rightarrow \mathbb{R}$ to predict anomalies. Ideally, $S(\mathbf{x})$ could approximate

the negative log-likelihood function, but since probability density functions often do not exist in \mathbb{R}^{d_0} , especially for image datasets, we estimate a score function $S_C : \mathbb{R}^{d+2} \rightarrow \mathbb{R}$ as the negative log-likelihood of the composite feature $\mathbf{z} = (E_{\phi_1}(\mathbf{x}), z_e(\mathbf{x}), z_c(\mathbf{x})) = C(\mathbf{x}) \in \mathbb{R}^{d+2}$, consisting of d latent features $\mathbf{z}_l \in \mathbb{R}^d$ and two reconstruction quality features $\mathbf{z}_r \in \mathbb{R}^2$ (squared error and cosine dissimilarity), where $\mathbf{z}_l = E_{\phi_1}(\mathbf{x})$ and $\mathbf{x}' = D_{\phi_2}(\mathbf{z}_l)$ are the latent and reconstruction from a pretrained AE or another pretrained network combined with PCA, $z_e(\mathbf{x}) = \frac{\|\mathbf{x} - \mathbf{x}'\|^2}{d_0}$ is the squared error of the reconstruction $\mathbf{x}' = D_{\phi_2}(E_{\phi_1}(\mathbf{x}))$, and $z_c(\mathbf{x}) = \frac{1}{2} \left(1 - \frac{\mathbf{x}^T \mathbf{x}'}{\|\mathbf{x}\| \|\mathbf{x}'\|} \right)$ is the cosine dissimilarity.

The distribution of composite features is denoted $p_d = C \# p_{d_0}$, which is obtained as a pushforward measure through the composite feature function C . (To simplify notation, distributions will be denoted by their probability density or mass functions for discrete random variables.)

The anomaly score function S_C is derived through noise contrastive estimation (NCE) [Gutmann and Hyvärinen, 2010, 2012]. In this process, an estimation network $T_{\theta}(\mathbf{u})$ is trained with supervision to predict whether the network's input \mathbf{u} is from the composite feature distribution p_d , such that $\mathbf{u} = \mathbf{z} = C(\mathbf{x}) \sim p_d$, or from a specified noise distribution p_n , such that $\mathbf{u} = \mathbf{v} \sim p_n$. After training, the optimized estimation network $T_{\theta^*}(\mathbf{z})$ approximates the log density ratio $\ln \frac{p_d(\mathbf{z})}{p_n(\mathbf{z})}$ plus a constant, which provides an approximation of the negative log-likelihood $-\ln p_d(\mathbf{z})$, since p_n is known. S_C is this approximation, such that a high $S(\mathbf{x}) = S_C(C(\mathbf{x}))$ suggests the data point \mathbf{x} is likely to be abnormal, while a low value indicates normality.

3.2 Autoencoder Network Design and Training

Autoencoders are designed to provide a compressed space of latent features, which can be used for anomaly detection as shown in previous work [Sakurada and Yairi, 2014, Sabokrou et al., 2018], and accurate reconstructions of normal data, while ideally providing poor reconstructions of anomalies. However, with vanilla training the latent feature distribution could create a degenerate distribution, i.e., the latent representations could contract to lie in a strict subspace of the whole latent space [Ozsoy et al., 2022], creating a singular covariance matrix. Non-degeneracy of the learned representations is necessary for the subsequent NCE as the contrastive noise is assumed to follow a multivariate Gaussian, and a degenerate distribution that lies in a subspace makes the problem ill-posed. To avoid the collapsed representation, we implement batch normalization directly before the latent space and penalize correlation among latent features in terms of the squared values of off-diagonal elements in the covariance matrix. Additionally, we adopt a decoupled training strategy to mitigate the impact of the covariance loss on the AE's ability to reconstruct input images. Specifically, the encoder is updated only during the first stage of training and is subsequently frozen in the second stage while the decoder is further trained. This decoupled training method also facilitates the learning of a higher-quality latent feature [Hu et al., 2024, Loaiza-Ganem et al., 2024], the details are in Appendix A. In summary, we propose to learn structured representations by training a constrained AE to jointly minimize the reconstruction error and a covariance loss term that encourages the components of the latent feature to be statistically uncorrelated.

As an alternative to using an AE, pretrained models can be employed to extract feature embeddings or latent representations. In line with the methodologies of [Bergmann et al., 2019, Reiss et al., 2021, Han et al., 2022], we utilize ResNet-18 [He et al., 2016], pretrained on ImageNet [Deng et al., 2009], to extract meaningful embedding after the last average pool layer. Given that the latent representation corresponding to features extracted by ResNet-18 are high-dimensional and the covariance matrix may be ill-conditioned, we further apply principal component analysis (PCA) to compress these features. Similar to the approach used with decoupled autoencoders, we concatenate the latent features and the reconstruction error features of the PCA to form the composite features.

Justification of Composite Feature Integration Although the advantages of employing composite features have been explored in prior discussions, this section provides a justification from the perspective of the VAE framework. The VAE is trained by maximizing the Evidence Lower Bound (ELBO), which serves as a lower bound on the data log-likelihood $\ln p_{d_0}(\mathbf{x})$. The ELBO objective

can be expressed as

$$\mathbb{E}_{\mathbf{x} \sim p_{d_0}} \left[\mathbb{E}_{q_{\phi_1}(\mathbf{z}_l|\mathbf{x})} [\ln q_{\phi_2}(\mathbf{x}|\mathbf{z}_l)] - D_{KL}(q_{\phi_1}(\mathbf{z}_l|\mathbf{x})\|p(\mathbf{z}_l)) \right], \quad (1)$$

where the first term represents the reconstruction loss, encouraging the model to accurately reconstruct the input data, and the second term acts as a regularization term, enforcing the approximate posterior distribution to be close to the prior $p(\mathbf{z}_l)$. Once the VAE is trained, several quantities derived from the model can serve as anomaly scores. These include the model likelihood $\mathbb{E}_{p(\mathbf{z}_l)}[q_{\phi_2}(\mathbf{x}|\mathbf{z}_l)]$, the reconstruction probability, $\mathbb{E}_{q_{\phi_1}(\mathbf{z}_l|\mathbf{x})} [\ln q_{\phi_2}(\mathbf{x}|\mathbf{z}_l)]$ [An and Cho, 2015], or the ELBO itself [Abati et al., 2019]. For training stability, it is common to model the decoder output as a Gaussian distribution $q_{\phi_2}(\mathbf{x}|\mathbf{z}_l) = \mathcal{N}(D_{\phi_2}(\mathbf{z}_l), \sigma^2 I)$. Under this assumption, $\ln q_{\phi_2}(\mathbf{x}|\mathbf{z}_l) \propto -\frac{1}{2\sigma^2} \|\mathbf{x} - D_{\phi_2}(\mathbf{z}_l)\|^2$. Substituting this into a negated ELBO (1) bound and setting $\sigma = 1/\sqrt{2}$, yields

$$\mathbb{E}_{q_{\phi_1}(\mathbf{z}_l|\mathbf{x})} [\|\mathbf{x} - D_{\phi_2}(\mathbf{z}_l)\|^2] + D_{KL}(q_{\phi_1}(\mathbf{z}_l|\mathbf{x})\|p(\mathbf{z}_l)), \quad (2)$$

which is minimized during training. If the encoder $q_{\phi_1}(\mathbf{z}_l|\mathbf{x})$ is deterministic, i.e., $q_{\phi_1}(\mathbf{z}_l|\mathbf{x}) = \delta(\mathbf{z}_l - E_{\phi_1}(\mathbf{x}))$, then the reconstruction term and KL divergence term¹ simplify to

$$\mathbb{E}_{q_{\phi_1}(\mathbf{z}_l|\mathbf{x})} [\|\mathbf{x} - D_{\phi_2}(\mathbf{z}_l)\|^2] = \|\mathbf{x} - D_{\phi_2}(E_{\phi_1}(\mathbf{x}))\|^2, \quad D_{KL}(q_{\phi_1}(\mathbf{z}_l|\mathbf{x})\|p(\mathbf{z}_l)) \propto -\ln p(E_{\phi_1}(\mathbf{x}))$$

Consequently, under the assumption of a deterministic encoder, the training loss in (2) reduces to $\|\mathbf{x} - D_{\phi_2}(E_{\phi_1}(\mathbf{x}))\|^2 - \ln p(E_{\phi_1}(\mathbf{x}))$. In LSA [Abati et al., 2019], the prior distribution $p(\mathbf{z}_l)$ is replaced with an autoregressive model p_r , resulting in the modified training loss,

$$\|\mathbf{x} - D_{\phi_2}(E_{\phi_1}(\mathbf{x}))\|^2 - \beta \ln p_r(E_{\phi_1}(\mathbf{x})), \quad (3)$$

where the above formula coincides with a deterministic encoder for the β -VAE [Higgins et al., 2017], which generalizes the standard VAE by introducing a hyperparameter β to scale the weight of the KL divergence term. During inference, the anomaly score is computed as the sum of the reconstruction error and the latent negative log-likelihood, with the former reflecting the model's memory capacity and the latter capturing the latent surprisal, which is (3) with $\beta = 1$.

In summary, the anomaly score in LSA builds upon both the reconstruction error and latent features, which corresponds to the ELBO of the data distribution when the VAE encoder is deterministic and the prior is modeled by a probabilistic model. By modeling the normalized reconstruction error $z_e = \|\mathbf{x} - D_{\phi_2}(E_{\phi_1}(\mathbf{x}))\|^2/d_0$ with an exponential-type likelihood, $p(z_e|\mathbf{z}_l) = d_0 e^{-d_0 z_e}$, the LSA anomaly score (3) can be interpreted as minimizing the negative log-likelihood of the joint distribution

$$\|\mathbf{x} - D_{\phi_2}(E_{\phi_1}(\mathbf{x}))\|^2 - \ln p_r(E_{\phi_1}(\mathbf{x})) \propto -\ln p(\mathbf{z}_l, z_e). \quad (4)$$

This interpretation not only provides a theoretical foundation for LSA but also justifies the principled learning of a joint distribution over latent feature and reconstruction error for the purpose of AD.

Similarly, to capture angular errors measured by the cosine dissimilarity of the reconstruction, the decoder output in a VAE can be modeled as a von Mises-Fisher distribution,

$$q_{\phi_2}(\mathbf{x}|\mathbf{z}_l) = C_d(\kappa) \exp \left(\kappa \frac{D_{\phi_2}(\mathbf{z}_l)^T \mathbf{x}}{\|D_{\phi_2}(\mathbf{z}_l)\| \|\mathbf{x}\|} \right), \quad \ln q_{\phi_2}(\mathbf{x}|\mathbf{z}_l) \propto -\frac{1}{2} \left(1 - \frac{D_{\phi_2}(\mathbf{z}_l)^T \mathbf{x}}{\|D_{\phi_2}(\mathbf{z}_l)\| \|\mathbf{x}\|} \right),$$

where $C_d(\kappa)$ denotes the normalizing constant and $\kappa = \frac{1}{2}$ in the second expression. Following the same reasoning used in the derivation of the anomaly score in LSA, we define a new anomaly score as $z_c = -\ln p_r(E_{\phi_1}(\mathbf{x}))$, which can be interpreted as the negative log-likelihood of the joint distribution $-\ln p(\mathbf{z}_l, z_c)$ under the same modeling assumptions as before, where $z_c = \frac{1}{2} \left(1 - \frac{\mathbf{x}^T \mathbf{x}'}{\|\mathbf{x}\| \|\mathbf{x}'\|} \right)$ represents the cosine dissimilarity between the input \mathbf{x} and the reconstructed input $\mathbf{x}' = D_{\phi_2}(E_{\phi_1}(\mathbf{x}))$.

These considerations demonstrate that modeling the joint distribution of latent feature \mathbf{z}_l with reconstruction error z_e and/or cosine dissimilarity z_c offers a principled and effective strategy for AD. Accordingly, we construct a composite feature $\mathbf{z} = (\mathbf{z}_l, z_e, z_c)$, consisting of the latent feature \mathbf{z}_l ,

¹The differential entropy of $\delta(\mathbf{z}_l - E_{\phi_1}(\mathbf{x}))$ is mathematically undefined (diverges to $-\infty$), but it is omitted here because it does not depend on the model parameters ϕ_1 or ϕ_2 . This simplification aligns with standard practice in deterministic encoder settings (e.g., regularized AEs), where only the prior-dependent term $-\ln p(E_{\phi_1}(\mathbf{x}))$ contributes to optimization gradients.

normalized reconstruction error z_e , and cosine dissimilarity z_c , to perform joint density estimation without assuming any specific parametric form such as an exponential-type likelihood, as was done in LSA. DAGMM also uses a composite feature based on the latent representation, but incorporates relative reconstruction error and cosine similarity instead of our reconstruction error and cosine dissimilarity (see Appendix H). Moreover, DAGMM performs density estimation using a GMM, which is restrictive parametric assumption compared to NCE.

3.3 Noise-Contrastive Estimation (NCE)

We adopt noise-contrastive estimation (NCE) [Gutmann and Hyvärinen, 2010, 2012] to train a neural network to produce an estimate of the probability density function p_d of the composite features z for normal data. The fundamental concept behind NCE is to model an unnormalized density function by contrasting it with an auxiliary noise distribution, which is intentionally designed to be tractable for both evaluation and sampling purposes. Given the data distribution p_d and the noise distribution p_n , we define the conditional distributions of u , which is either data or noise, as $p_{u|y}(u|y) = \begin{cases} p_d(u), & y = 1 \\ p_n(u), & y = 0 \end{cases}$, where $y \in \{0, 1\}$. Then, the model distribution p_z^θ is indirectly fit to the data distribution p_d using the maximum likelihood estimate of $p_{y|u}^\theta$ as

$$\max_{\theta} \mathbb{E}[\ln p_{y|u}^\theta(y|u)] = \max_{\theta} \mathbb{E}_{z \sim p_d} [\ln p_{y|z}^\theta(1|z)] + \nu \mathbb{E}_{v \sim p_n} [\ln p_{y|z}^\theta(0|v)], \quad (5)$$

where ν denotes $\frac{\Pr(y=0)}{\Pr(y=1)}$. The posterior probability $p_{y|u}^\theta$ is modeled using logistic regression

$$p_{y|u}^\theta(y=1|u) = \frac{p_z^\theta(u)}{p_z^\theta(u) + \nu p_n(u)} = \sigma(\ln p_z^\theta(u) - \ln \nu p_n(u)) = \sigma(T_\theta(u)),$$

where $\sigma(x) = \frac{1}{1+e^{-x}}$ is the sigmoid function and T_θ is a neural network model of the log-odds $\ln p_z^\theta(u) - \ln \nu p_n(u)$. Substituting the expressions of $p_{y|u}^\theta(1|u)$ and $p_{y|u}^\theta(0|u) = 1 - p_{y|u}^\theta(1|u)$ in terms of T_θ into (5), and negating the objective we obtain the loss function

$$\mathcal{L}_{\text{NCE}}(\theta) = - \mathbb{E}_{z \sim p_d} [\ln \sigma(T_\theta(z))] - \nu \mathbb{E}_{v \sim p_n} [\ln(1 - \sigma(T_\theta(v)))] . \quad (6)$$

Substituting θ^* , the minimizer of $\mathcal{L}_{\text{NCE}}(\theta)$, into the log-odds and rearranging the terms yields $\ln p_z^{\theta^*}(z) = T_{\theta^*}(z) + \ln \nu p_n(z) = -S_C(z)$, where S_C is the anomaly score on the composite features. When the model is sufficiently powerful, the optimal model $p_{y|u}^{\theta^*}$ will match $p_{y|u}$, implying that $p_z^{\theta^*} \equiv p_d$ and $S_C(z) \equiv -\ln p_d(z)$.

3.4 Adapting NCE for Anomaly Detection

Selecting an appropriate noise distribution $p_n(z)$ is crucial for the success of NCE. As discussed in [Gutmann and Hyvärinen, 2010], NCE performs optimally when the noise distribution p_n closely resembles the composite feature distribution p_d . Following this principle, we iteratively optimize the noise distribution during NCE training.

Optimizing Noise Distribution In NCE, the noise distribution p_n is often chosen to be Gaussian $\mathcal{N}(\hat{\mu}_z, \hat{\Sigma}_z)$, where $\hat{\mu}_z$ and $\hat{\Sigma}_z$ are the sample mean and variance derived from the training dataset, respectively.² We create a refined noise distribution for NCE through the parametrization $p_{nK} = \mathcal{N}(\hat{\mu}_z, K^T \hat{\Sigma}_z K)$, where K represents a parameter matrix. Subsequently, reparameterization trick makes it feasible to optimize K to maximize the NCE loss through backpropagation. We first draw a sample $z \sim \mathcal{N}(\hat{\mu}_z, \hat{\Sigma}_z)$ and then use the affine function $L_K(z) = K(z - \hat{\mu}_z) + \hat{\mu}_z$ to draw from the intended Gaussian $\mathcal{N}(\hat{\mu}_z, K^T \hat{\Sigma}_z K)$. However, the naive maximization of the NCE loss in terms of K is equivalent to minimizing $\mathbb{E}_{u \sim p_n} [\ln(1 - \sigma(T_\theta(L_K(u))))]$, since the first term in (6) does not

²For large training datasets, these two estimators are not feasible because the entire dataset cannot be processed by the compression network simultaneously. To address this limitation, we can iteratively estimate the mean and covariance of the sample in batches as detailed in Appendix B.

depend on noise. Instead, following similar work for GAN training [Che et al., 2016], the first term in the NCE loss can be incorporated into the optimization as

$$\min_{\mathbf{K}} \mathbb{E}_{\mathbf{u} \sim p_d} [\ln \sigma (T_{\theta} (L_{\mathbf{K}} (\mathbf{sg} (L_{\mathbf{K}}^{-1} (\mathbf{u})))))] + \nu \mathbb{E}_{\mathbf{u} \sim p_n} [\ln (1 - \sigma (T_{\theta} (L_{\mathbf{K}} (\mathbf{u}))))], \quad (7)$$

where $L_{\mathbf{K}}^{-1}(\mathbf{z}) = \mathbf{K}^{-1}(\mathbf{z} - \hat{\mu}_{\mathbf{z}}) + \hat{\mu}_{\mathbf{z}}$ and $\mathbf{sg}(\cdot)$ is the stop gradient operation.

Augmenting Reconstruction Features for Normal Data Well-chosen data augmentation techniques generally enhance model performance. However, in anomaly detection augmentations that preserve normality require domain knowledge. We propose to augment normal data by adjusting the reconstruction features alone, without modifying the input or latent representations.³ We achieve this by generating additional normal points by replacing reconstruction features with artificially lower values while maintaining the latent representations. The goal is to bias the estimation network such that artificially low reconstruction features, which may be observed by chance in points the noise distribution, are deemed normal.

Specifically, we create artificial normal points by defining $\mathbf{z} = (\mathbf{z}_l, \mathbf{z}'_e, \mathbf{z}'_c)$, where \mathbf{z}_l is the latent feature of normal data, and $\mathbf{z}'_e \sim p_{t_1}$ and $\mathbf{z}'_c \sim p_{t_2}$ are independently drawn from the truncated normal distributions. Next, we explain how the parameters of the truncated normal distributions p_{t_1} and p_{t_2} are defined to ensure that each marginals of the augmented data distribution have a density that is higher than the noise distribution over low reconstruction errors/dissimilarities.

Given that the reconstruction feature exhibits a skewed unimodal form, we assume it follows a log-normal distribution, $\ln z \sim \mathcal{N}(\mu, \sigma)$, where $z \sim p_t$ is either $z_e \sim p_{t_1}$ or $z_c \sim p_{t_2}$. For a log-normal distribution, the mode m_z can be expressed in terms of the mean μ_z and variance σ_z^2 as $m_z = \mu_z (\frac{\sigma_z^2}{\mu_z^2} + 1)^{-\frac{3}{2}}$, as derived in Appendix C. Therefore, we compute distribution mean μ_z and distribution variance σ_z^2 using the training dataset and apply the derived formula to estimate the mode m_z . The estimated mode is then used to define the truncated normal distribution p_t defined on $[0, m_z]$.

Let A be a latent indicator variable, where $A = 1$ corresponds to the original normal data component and $A = 0$ to the artificial normal component. Since we consider an equal mixture of both types of points, we set $A \sim \text{Ber}(\frac{1}{2})$. The augmented density function is then given by

$$p_m(\mathbf{z}) = \sum_A p(A)p(\mathbf{z}|A) = \frac{1}{2}p_d(\mathbf{z}) + \frac{1}{2}p_l(\mathbf{z}_l)p_{t_1}(\mathbf{z}_e)p_{t_2}(\mathbf{z}_c), \quad (8)$$

where p_l represents the marginal distribution of p_d with respect to the latent feature \mathbf{z}_l , and p_{t_1} and p_{t_2} are the truncated normal distributions for the reconstruction features \mathbf{z}_e and \mathbf{z}_c , respectively. p_m is substituted for p_d in (6) during the optimization of the estimation network. The following proposition (proof in Appendix D) provides a quantitative justification for the data augmentation strategy.

Proposition 1 *The density of the marginal distribution of the reconstruction feature in p_m is no less than the density of the corresponding marginal distribution of the noise distribution p_n over the interval $[0, m_z]$.*

Implementation Taking into account the parameterized noise distribution, we adopt an alternating optimization strategy with the batch loss for the estimation network T_{θ} as

$$\hat{\mathcal{L}}_{\text{CANCE}}(\theta) = -\frac{1}{M} \sum_{i=1}^M \ln \sigma (T_{\theta}(\mathbf{z}_i)) - \frac{\nu}{N} \sum_{i=1}^N \ln (1 - \sigma (T_{\theta} (L_{\mathbf{K}} (\mathbf{v}_i)))), \quad (9)$$

where $\nu = \frac{N}{M}$ is the noise-sample ratio, $\mathbf{z}_1, \dots, \mathbf{z}_M$ is sampled from the augmented data $\mathbf{z}_i \sim p_m$ and $\mathbf{v}_1, \dots, \mathbf{v}_N$ is sampled from the noise distribution $\mathbf{v}_i \sim p_n$. The corresponding batch loss version of (7) is used to update \mathbf{K} ,

$$-\frac{1}{M} \sum_{i=1}^M \ln \sigma (T_{\theta} (L_{\mathbf{K}} (\mathbf{sg} (L_{\mathbf{K}}^{-1} (\mathbf{z}_i))))) - \frac{\nu}{N} \sum_{i=1}^N \ln (1 - \sigma (T_{\theta} (L_{\mathbf{K}} (\mathbf{v}_i)))), \quad (10)$$

³Data augmentation of the input improves model performance [Golan and El-Yaniv, 2018], but it is beyond the scope of this paper, as our model and other baselines do not incorporate it.

Furthermore, we constrain \mathbf{K} to be a diagonal matrix with diagonal elements equal to or greater than 1. This constraint enhances training stability (noise variance can only grow) and facilitates a more efficient computation of the inverse of the affine transformation $L_{\mathbf{K}}$. In practice, the constraint is enforced via softplus $K_{jj} = 1 + \log(1 + \exp(\psi_j))$, $\psi \in \mathbb{R}^d$. AdamW is used for both sets of parameters θ and ψ .

4 Experiments

We use standard benchmark datasets to empirically assess the effectiveness of our proposed method in unsupervised anomaly detection tasks. **MNIST** [LeCun et al., 2010] is a grayscale image dataset with 10 classes containing digits from 0 to 9. It consists of 60,000 training images and 10,000 test images, each 28×28 pixels. **MNIST-C** [Mu and Gilmer, 2019] is a comprehensive suite of 15 corruptions applied to the MNIST test set (along with the original set), for benchmarking out-of-distribution robustness in computer vision. **CIFAR-10** [Krizhevsky et al., 2010] is a color image dataset with 10 classes. It includes 50,000 training images and 10,000 test images, each 32×32 pixels. **Fashion-MNIST** [Xiao et al., 2017] is a grayscale image dataset of clothing items organized similar to MNIST.

We also validate test three tabular dataset: Abalone, Thyroid, and Arrhythmia. Consistent with previous research [Zong et al., 2018, Goyal et al., 2020, Fu et al., 2024], we utilize the F1-score to compare the methods and adhere to their guidelines in preparing the dataset.

Following prior work [Abati et al., 2019], we use the labeled image datasets to create **unimodal** anomaly datasets where one class is normal and the rest as anomalies. Only normal data in the training set is seen during training and model selection. The whole test dataset is employed at testing. For **multimodal** datasets, two or more classes are considered normal. Again, data from these classes in the training set is used for training and the entire test set is for testing. Finally, for MNIST-C we adopt the settings from [Lee and Lee, 2023]: the entire MNIST training dataset is used for model training, while the MNIST-C [Mu and Gilmer, 2019] dataset is utilized for testing, such that the original MNIST images are considered normal and corrupted images in MNIST-C are deemed abnormal. The anomaly detection performance is evaluated using the Area Under the Receiver Operating Characteristic Curve (AUROC), as is common in prior work [Abati et al., 2019, Ruff et al., 2018]. We perform each experiment five times and report the mean and the standard deviation.

4.1 Ablation Study

We conduct an ablation study to evaluate the contributions of the individual components of the proposed method designated as follows: **Error** uses only the AE’s error as the anomaly score, **LatNCE** uses NCE on the AE’s latent features, **CNCE** uses NCE on the composite features, and **CANCE** method uses NCE on the composite features trained with augmented reconstruction features.

The results for the unimodal cases of MNIST and CIFAR-10 datasets and the multimodal MNIST-C are summarized in Table 1 with full results for unimodal in Table 7 and additional bimodal cases in Table 8 in Appendix F. In almost all cases, CNCE achieves higher AUROC values than Error, which highlights the importance of latent features. Moreover, CNCE consistently outperforms LatNCE. Finally, CANCE performs slightly better than CNCE (equal or better mean performance on 17 of the 20 unimodal datasets, the 7 multimodal datasets).

Table 1: Ablation study

Data	Error	LatNCE	CNCE	CANCE
MNIST	95.1	84.1	97.0	97.7
CIFAR-10	54.1	65.1	65.3	65.4
MNIST-C	89.7 ± 0.5	78.4 ± 1.4	91.3 ± 0.4	92.2 ± 0.4

Results on Unimodal MNIST and CIFAR-10 We compare against the following baseline methods that they are similar to CANCE in that they use probability models and/or reconstruction models with minimal data pre-processing: KDE: Kernel Density Estimator after PCA-whitening; VAE: variational autoencoder [Kingma and Welling, 2013], Evidence Lower Bound (ELBO) is anomaly

score; Pix-CNN [Van den Oord et al., 2016] uses density modeling by autoregression in the image space; LSA: Latent Space Autoregression [Abati et al., 2019]; DAGMM [Zong et al., 2018] uses composite features using latent representation and reconstruction feature with density estimation performed by jointly training an AE and Gaussian mixture model. Except for the last two methods, AUROC values on MNIST and CIFAR-10 are extracted from previous literature [Abati et al., 2019]. Since DAGMM is not evaluated on MNIST and CIFAR-10 in [Zong et al., 2018], we use the same architecture as our method. In all cases, the model is trained for 400 epochs with a fixed learning rate of 10^{-4} , and the number of Gaussians within the model is set to 4. The best model is saved when the lowest validation loss is achieved. However, on CIFAR-10, we have encountered issues with degenerated covariance matrices in the DAGMM. Therefore, we have changed the latent dimension from 64 to 16. In the process of implementing DAGMM, we find that DAGMM does not train stably if the latent dimension or the number of Gaussians within the model is not properly set up. We also perform an additional comparison with DAGMM using the same dataset and neural network. The results and analysis are provided in Appendix H.

Table 2: AUCROC [%] for baseline methods, Pix-CNN (PC) and DAGMM, compared to CANCE mean and std. value across 5 independent runs.

Data	KDE	VAE	PC	LSA	DAGMM	CANCE
MNIST	81.4	96.9	61.8	97.5	53.1	97.7
CIFAR-10	61.0	58.6	55.1	64.1	47.7	65.4

As shown in Table 2, our proposal outperforms all baselines tested across both datasets, Table 10 in Appendix G details the AUROC performance of each method. All methods except DAGMM and Pix-CNN perform favorably on MNIST. DAGMM completely fails because it is not designed for image dataset, as noted in other work [Hojjati and Armanfard, 2023]. Pix-CNN struggles to model distributions, which partly supports our previous argument that the true effective dimensionality is significantly smaller than the image dimensionality, and thus data density functions may not exist in image space. Notably, the deep probability models, including VAE, LSA, and CANCE, achieve better performance than KDE on MNIST, but CIFAR-10 presents a much greater challenge due to the higher diversity of classes and the complex backgrounds in which the class objects are depicted.

Results on Multimodal MNIST-C For the MNIST-C dataset, we compare CANCE to SVDD [Tax and Duin, 2004], Deep SVDD [Ruff et al., 2018], and Deep SAD [Ruff et al., 2019], which were previously reported in Table 3 of [Lee and Lee, 2023] and DROCC [Goyal et al., 2020]. For CANCE, we use the same network structure and hyperparameters as in the unimodal case, except for increasing the latent dimension from 6 to 10 to accommodate the more complex training dataset consisting of 10 class/‘modes’. We also execute DROCC, a state-of-the-art method, 30 times as the baseline. For the network architecture, we adapt the published version used by DROCC for CIFAR-10, with the following modifications: changing the input image channel from 3 to 1 and adjusting the latent dimension from 128 to 32. The testing results are shown in Table 3. CANCE and DROCC are comparable and outperform other methods.

Table 3: Anomaly detection on MNIST-C, AUROC over 30 runs

SVDD	DSVDD	DSAD	DROCC	CANCE
67.6	82.8	84.0	92.3 ± 1.9	92.2 ± 0.4

Results on CIFAR-10 and Fashion-MNIST using ResNet-18 as Feature Extractor To demonstrate the generality of our method, we also tested it using a pretrained ResNet-18, followed by PCA, to prepare the composite feature and perform density estimation as previously conducted. (An ablation study on unimodal datasets is included as Table 9 in the Appendix F.)

Table 4: AUROC[%] on CIFAR-10 for baseline methods. Nearest neighbor (NN) baseline uses either original space or like CANCE the ResNet-18 features.

Data	DSVDD	NN	DROCC	DPAD	CANCE
CIFAR-10	64.8	59.5 79.1	74.2	74.5	88.0

The comparison versus baselines is shown in Table 4, with detailed results in Table 11 in Appendix G. CANCE on top of ResNet-18 has much higher performance than an AE space, outperforming other methods by a wide margin and achieving state-of-the-art performance. We see an improved performance using ResNet-18 features for the nearest neighbor (NN) baseline too, which was shown to be the second best method to DROCC [Goyal et al., 2020]. We also test on Fashion-MNIST and CIFAR-10 in a multimodal setting, where one class is treated as anomalous and the remaining nine as normal. This results in 10 experiments per dataset. We compare our method with DeepSVDD, DROCC, and DPAD, with average performance reported in Table 5. It should be noted that we did not train DROCC or DPAD [Fu et al., 2024] on the ResNet-18 representation.

Table 5: Average AUROC (9 vs 1) on Fashion-MNIST and CIFAR-10

Method	DeepSVDD	DROCC	DPAD	CANCE
Fashion-MNIST	65.9	54.8	70.2	70.6
CIFAR-10	52.3	54.3	66.1	65.5

Results on Tabular Data On tabular data, CANCE outperforms the previous methods by a wide margin on Abalone, and is comparable to DROCC and better than DeepSVDD and GOAD [Bergman and Hoshen, 2020] on Thyroid. However, results on the small Arrhythmia dataset are note competitive. This limitation of CANCE arises when the dataset is small but the dimensionality is high, as AE may fail to learn meaningful composite features under such conditions.

Table 6: Performance of AD Methods on Tabular Data. Baselines from Fu et al. [2024] (first and last rows) and Goyal et al. [2020] (second row).

Method	DAGMM	DeepSVDD	GOAD	DROCC	DPAD	CANCE
Abalone	0.20 ± 0.03	0.62 ± 0.01	0.61 ± 0.02	0.68 ± 0.02	0.67 ± 0.02	0.83 ± 0.06
Thyroid	0.49 ± 0.04	0.73 ± 0.00	0.72 ± 0.01	0.78 ± 0.03	-	0.77 ± 0.01
Arrhythmia	0.49 ± 0.03	0.54 ± 0.01	0.51 ± 0.02	0.32 ± 0.02	0.67 ± 0.00	0.59 ± 0.02

5 Conclusion

In this work, we propose an innovative approach for detecting anomalies within an unsupervised learning framework. Our approach is motivated by modeling the joint distribution of an auto-encoders latent features and reconstruction errors, and we use innovations on noise contrastive estimation to estimate the likelihood function. Experimental evaluations on multiple benchmark datasets demonstrate that our proposed approach matches the performance of leading state-of-the-art anomaly detection algorithms, and in contrast to other complex deep probability models, our method is relatively straightforward to implement. As PCA is a linear autoencoder, our approach can be applied to embeddings from pretrained neural network representations. This makes the method potentially applicable to a variety of domains, including vision-language models.

References

Davide Abati, Angelo Porrello, Simone Calderara, and Rita Cucchiara. Latent space autoregression for novelty detection. In *Proceedings of the IEEE/CVF Conference on Computer Vision and Pattern Recognition*, pages 481–490, 2019.

Jinwon An and Sungzoon Cho. Variational autoencoder based anomaly detection using reconstruction probability. *Special Lecture on IE*, 2(1):1–18, 2015.

Jerome TA Andrews, Edward J Morton, and Lewis D Griffin. Detecting anomalous data using auto-encoders. *International Journal of Machine Learning and Computing*, 6(1):21, 2016.

Liron Bergman and Yedid Hoshen. Classification-based anomaly detection for general data. *arXiv preprint arXiv:2005.02359*, 2020.

Paul Bergmann, Michael Fauser, David Sattlegger, and Carsten Steger. Mvttec ad—a comprehensive real-world dataset for unsupervised anomaly detection. In *Proceedings of the IEEE/CVF Conference on Computer Vision and Pattern Recognition*, pages 9592–9600, 2019.

Christopher M Bishop. Novelty detection and neural network validation. *IEE Proceedings-Vision, Image and Signal Processing*, 141(4):217–222, 1994.

Varun Chandola, Arindam Banerjee, and Vipin Kumar. Anomaly detection: A survey. *ACM Computing Surveys (CSUR)*, 41(3):1–58, 2009.

Tong Che, Yanran Li, Athul Paul Jacob, Yoshua Bengio, and Wenjie Li. Mode regularized generative adversarial networks. *arXiv preprint arXiv:1612.02136*, 2016.

Zhaomin Chen, Chai Kiat Yeo, Bu Sung Lee, and Chiew Tong Lau. Autoencoder-based network anomaly detection. In *2018 Wireless Telecommunications Symposium (WTS)*, pages 1–5. IEEE, 2018.

Hyunsun Choi, Eric Jang, and Alexander A Alemi. Waic, but why? generative ensembles for robust anomaly detection. *arXiv preprint arXiv:1810.01392*, 2018.

Jia Deng, Wei Dong, Richard Socher, Li-Jia Li, Kai Li, and Li Fei-Fei. Imagenet: A large-scale hierarchical image database. In *2009 IEEE Conference on Computer Vision and Pattern Recognition*, pages 248–255. Ieee, 2009.

Federico Di Mattia, Paolo Galeone, Michele De Simoni, and Emanuele Ghelfi. A survey on gans for anomaly detection. *arXiv preprint arXiv:1906.11632*, 2019.

Dazhi Fu, Zhao Zhang, and Jicong Fan. Dense projection for anomaly detection. In *Proceedings of the AAAI Conference on Artificial Intelligence*, volume 38, pages 8398–8408, 2024.

Izhak Golan and Ran El-Yaniv. Deep anomaly detection using geometric transformations. *Advances in Neural Information Processing Systems*, 31, 2018.

Ian Goodfellow, Jean Pouget-Abadie, Mehdi Mirza, Bing Xu, David Warde-Farley, Sherjil Ozair, Aaron Courville, and Yoshua Bengio. Generative adversarial nets. *Advances in Neural Information Processing Systems*, 27, 2014.

Sachin Goyal, Aditi Raghunathan, Moksh Jain, Harsha Vardhan Simhadri, and Prateek Jain. Droc: Deep robust one-class classification. In *International Conference on Machine Learning*, pages 3711–3721. PMLR, 2020.

Michael Gutmann and Aapo Hyvärinen. Noise-contrastive estimation: A new estimation principle for unnormalized statistical models. In *Proceedings of the Thirteenth International Conference on Artificial Intelligence and Statistics*, pages 297–304. JMLR Workshop and Conference Proceedings, 2010.

Michael U Gutmann and Aapo Hyvärinen. Noise-contrastive estimation of unnormalized statistical models, with applications to natural image statistics. *Journal of Machine Learning Research*, 13(2), 2012.

Songqiao Han, Xiyang Hu, Hailiang Huang, Minqi Jiang, and Yue Zhao. Adbench: Anomaly detection benchmark. *Advances in Neural Information Processing Systems*, 35:32142–32159, 2022.

Kaiming He, Xiangyu Zhang, Shaoqing Ren, and Jian Sun. Deep residual learning for image recognition. In *Proceedings of the IEEE Conference on Computer Vision and Pattern Recognition*, pages 770–778, 2016.

Irina Higgins, Loic Matthey, Arka Pal, Christopher Burgess, Xavier Glorot, Matthew Botvinick, Shakir Mohamed, and Alexander Lerchner. beta-vae: Learning basic visual concepts with a constrained variational framework. In *International conference on learning representations*, 2017.

Hadi Hojjati and Narges Armanfard. Dasvdd: Deep autoencoding support vector data descriptor for anomaly detection. *IEEE Transactions on Knowledge and Data Engineering*, 2023.

Tianyang Hu, Fei Chen, Haonan Wang, Jiawei Li, Wenjia Wang, Jiacheng Sun, and Zhenguo Li. Complexity matters: Rethinking the latent space for generative modeling. *Advances in Neural Information Processing Systems*, 36, 2024.

Diederik P Kingma and Max Welling. Auto-encoding variational bayes. *arXiv preprint arXiv:1312.6114*, 2013.

Durk P Kingma and Prafulla Dhariwal. Glow: Generative flow with invertible 1x1 convolutions. *Advances in Neural Information Processing Systems*, 31, 2018.

Alex Krizhevsky, Vinod Nair, and Geoffrey Hinton. Cifar-10 (canadian institute for advanced research). *URL http://www.cs.toronto.edu/kriz/cifar.html*, 5(4):1, 2010.

Yann LeCun, Corinna Cortes, Chris Burges, et al. Mnist handwritten digit database, 2010.

Chong Hyun Lee and Kibae Lee. Semi-supervised anomaly detection algorithm based on kl divergence (sad-kl). In *Anomaly Detection and Imaging with X-Rays (ADIX) VIII*, volume 12531, pages 118–123. SPIE, 2023.

Gabriel Loaiza-Ganem, Brendan Leigh Ross, Rasa Hosseinzadeh, Anthony L Caterini, and Jesse C Cresswell. Deep generative models through the lens of the manifold hypothesis: A survey and new connections. *arXiv preprint arXiv:2404.02954*, 2024.

Luke Metz, Ben Poole, David Pfau, and Jascha Sohl-Dickstein. Unrolled generative adversarial networks. *arXiv preprint arXiv:1611.02163*, 2016.

Norman Mu and Justin Gilmer. Mnist-c: A robustness benchmark for computer vision. *arXiv preprint arXiv:1906.02337*, 2019.

Eric Nalisnick, Akihiro Matsukawa, Yee Whye Teh, Dilan Gorur, and Balaji Lakshminarayanan. Do deep generative models know what they don't know? *arXiv preprint arXiv:1810.09136*, 2018.

Serdar Ozsoy, Shadi Hamdan, Sercan Arik, Deniz Yuret, and Alper Erdogan. Self-supervised learning with an information maximization criterion. *Advances in Neural Information Processing Systems*, 35:35240–35253, 2022.

Emanuel Parzen. On estimation of a probability density function and mode. *The Annals of Mathematical Statistics*, 33(3):1065–1076, 1962.

Tal Reiss, Niv Cohen, Liron Bergman, and Yedid Hoshen. Panda: Adapting pretrained features for anomaly detection and segmentation. In *Proceedings of the IEEE/CVF Conference on Computer Vision and Pattern Recognition*, pages 2806–2814, 2021.

Jie Ren, Peter J Liu, Emily Fertig, Jasper Snoek, Ryan Poplin, Mark Depristo, Joshua Dillon, and Balaji Lakshminarayanan. Likelihood ratios for out-of-distribution detection. *Advances in Neural Information Processing Systems*, 32, 2019.

Lukas Ruff, Robert Vandermeulen, Nico Goernitz, Lucas Deecke, Shoaib Ahmed Siddiqui, Alexander Binder, Emmanuel Müller, and Marius Kloft. Deep one-class classification. In *International Conference on Machine Learning*, pages 4393–4402. PMLR, 2018.

Lukas Ruff, Robert A Vandermeulen, Nico Görnitz, Alexander Binder, Emmanuel Müller, Klaus-Robert Müller, and Marius Kloft. Deep semi-supervised anomaly detection. *arXiv preprint arXiv:1906.02694*, 2019.

Lukas Ruff, Jacob R Kauffmann, Robert A Vandermeulen, Grégoire Montavon, Wojciech Samek, Marius Kloft, Thomas G Dietterich, and Klaus-Robert Müller. A unifying review of deep and shallow anomaly detection. *Proceedings of the IEEE*, 109(5):756–795, 2021.

Mohammad Sabokrou, Mohsen Fayyaz, Mahmood Fathy, Zahra Moayed, and Reinhard Klette. Deep-anomaly: Fully convolutional neural network for fast anomaly detection in crowded scenes. *Computer Vision and Image Understanding*, 172:88–97, 2018.

Mayu Sakurada and Takehisa Yairi. Anomaly detection using autoencoders with nonlinear dimensionality reduction. In *Proceedings of the MLSDA 2014 2nd Workshop on Machine Learning for Sensory Data Analysis*, pages 4–11, 2014.

Tim Salimans, Andrej Karpathy, Xi Chen, and Diederik P Kingma. Pixelcnn++: Improving the pixelcnn with discretized logistic mixture likelihood and other modifications. *arXiv preprint arXiv:1701.05517*, 2017.

Thomas Schlegl, Philipp Seeböck, Sebastian M Waldstein, Ursula Schmidt-Erfurth, and Georg Langs. Unsupervised anomaly detection with generative adversarial networks to guide marker discovery. In *International Conference on Information Processing in Medical Imaging*, pages 146–157. Springer, 2017.

Philipp Seeböck, Sebastian Waldstein, Sophie Klimscha, Bianca S Gerendas, René Donner, Thomas Schlegl, Ursula Schmidt-Erfurth, and Georg Langs. Identifying and categorizing anomalies in retinal imaging data. *arXiv preprint arXiv:1612.00686*, 2016.

David MJ Tax and Robert PW Duin. Support vector data description. *Machine Learning*, 54:45–66, 2004.

Aaron Van den Oord, Nal Kalchbrenner, Lasse Espeholt, Oriol Vinyals, Alex Graves, et al. Conditional image generation with pixelcnn decoders. *Advances in Neural Information Processing Systems*, 29, 2016.

Yan Xia, Xudong Cao, Fang Wen, Gang Hua, and Jian Sun. Learning discriminative reconstructions for unsupervised outlier removal. In *Proceedings of the IEEE International Conference on Computer Vision*, pages 1511–1519, 2015.

Han Xiao, Kashif Rasul, and Roland Vollgraf. Fashion-mnist: a novel image dataset for benchmarking machine learning algorithms. *arXiv preprint arXiv:1708.07747*, 2017.

Dan Xu, Elisa Ricci, Yan Yan, Jingkuan Song, and Nicu Sebe. Learning deep representations of appearance and motion for anomalous event detection. *arXiv preprint arXiv:1510.01553*, 2015.

Haowen Xu, Wenxiao Chen, Nengwen Zhao, Zeyan Li, Jiahao Bu, Zhihan Li, Ying Liu, Youjian Zhao, Dan Pei, Yang Feng, et al. Unsupervised anomaly detection via variational auto-encoder for seasonal kpis in web applications. In *Proceedings of the 2018 World Wide Web Conference*, pages 187–196, 2018.

Sangwoong Yoon, Young-Uk Jin, Yung-Kyun Noh, and Frank Park. Energy-based models for anomaly detection: A manifold diffusion recovery approach. *Advances in Neural Information Processing Systems*, 36, 2024.

Houssam Zenati, Chuan Sheng Foo, Bruno Lecouat, Gaurav Manek, and Vijay Ramaseshan Chandrasekhar. Efficient gan-based anomaly detection. *arXiv preprint arXiv:1802.06222*, 2018.

Shuangfei Zhai, Yu Cheng, Weining Lu, and Zhongfei Zhang. Deep structured energy based models for anomaly detection. In *International Conference on Machine Learning*, pages 1100–1109. PMLR, 2016.

Bo Zong, Qi Song, Martin Renqiang Min, Wei Cheng, Cristian Lumezanu, Daeki Cho, and Haifeng Chen. Deep autoencoding gaussian mixture model for unsupervised anomaly detection. In *International Conference on Learning Representations*, 2018.

A Autoencoder Training

The loss function that guides training of the compression networks encoder and decoder parameters, ϕ_1 and ϕ_2 , respectively, is $\mathcal{L}(\phi_1, \phi_2) = \mathcal{L}_{error}(\phi_1, \phi_2) + \lambda \mathcal{L}_{cov}(\phi_1)$ with trade-off hyperparameter λ between the two losses

$$\mathcal{L}_{error}(\phi_1, \phi_2) = \mathbb{E}_{\mathbf{x} \sim p_{d_0}} [\|\mathbf{x} - D_{\phi_2}(E_{\phi_1}(\mathbf{x}))\|^2], \quad (11)$$

$$\mathcal{L}_{cov}(\phi_1) = \frac{1}{d(d-1)} \left\| \text{off}(\Sigma_{E_{\phi_1}(\mathbf{x})}) \right\|_F^2, \quad (12)$$

where $\mathcal{L}_{error}(\phi_1, \phi_2)$ is the mean squared error of the reconstruction, $\mathcal{L}_{cov}(\phi_1)$ is the mean of the squared off-diagonal elements in the covariance matrix $\Sigma_{E_{\phi_1}(\mathbf{x})}$ of the latent representation $\mathbf{z}_l = E_{\phi_1}(\mathbf{x})$, $\text{off}(\Sigma) = \Sigma - \Sigma \odot \mathbf{I}_d$, \odot is the element-wise product, and \mathbf{I}_d is the identity matrix.

The primary goal of incorporating the covariance loss $\mathcal{L}_{cov}(\phi_1)$ into the AE's loss is to maintain the non-singularity of $\Sigma_{E_{\phi_1}(\mathbf{x})}$. In NCE, the noise distribution typically follows a Gaussian, with its mean and covariance derived from the training dataset. When the covariance matrix $\Sigma_{E_{\phi_1}(\mathbf{x})}$ is singular degenerate, it corresponds to a degenerate distribution and lacks a density. Furthermore, if the covariance matrix is ill-conditioned it causes numerical issues during the computation of the covariance matrix's inverse. Consequently, the goal is to simply choose the smallest λ that yields a well-conditioned covariance.

Additionally, we adopt a decoupled training strategy to mitigate the impact of the covariance loss on the AE's ability to reconstruct input images. Specifically, the encoder is updated only during the first stage of training and is subsequently frozen in the second stage while the decoder is further trained. This decoupled training method also facilitates the learning of a higher-quality latent feature [Hu et al., 2024, Loaiza-Ganem et al., 2024].

B Mean and Variance Derivation

By the definition of the sample mean, we have

$$\begin{aligned} \hat{\mu}_{\mathbf{z}}^{(t+1)} &= \frac{1}{n_t + n_b} \sum_{i=1}^{n_t + n_b} \mathbf{z}_i \\ &= \frac{1}{n_t + n_b} \left(\sum_{i=1}^{n_t} \mathbf{z}_i + \sum_{i=n_t+1}^{n_t + n_b} \mathbf{z}_i \right) \\ &= \frac{n_t \hat{\mu}_{\mathbf{z}}^{(t)} + n_b \hat{\mu}_{\mathbf{z}}^{(b)}}{n_t + n_b} \end{aligned} \quad (13)$$

By definition, the sample covariance matrix is as follows:

$$\begin{aligned} \hat{\Sigma}_{\mathbf{z}}^{(t+1)} &= \frac{1}{n_t + n_b} \sum_{i=1}^{n_t + n_b} \left(\mathbf{z}_i - \hat{\mu}_{\mathbf{z}}^{(t+1)} \right)^T \left(\mathbf{z}_i - \hat{\mu}_{\mathbf{z}}^{(t+1)} \right) \\ &= \frac{1}{n_t + n_b} \left[\sum_{i=1}^{n_t} \left(\mathbf{z}_i - \hat{\mu}_{\mathbf{z}}^{(t+1)} \right)^T \left(\mathbf{z}_i - \hat{\mu}_{\mathbf{z}}^{(t+1)} \right) + \sum_{i=n_t+1}^{n_t + n_b} \left(\mathbf{z}_i - \hat{\mu}_{\mathbf{z}}^{(t+1)} \right)^T \left(\mathbf{z}_i - \hat{\mu}_{\mathbf{z}}^{(t+1)} \right) \right] \end{aligned}$$

Consider expanding the first sum term as follows,

$$\begin{aligned}
& \sum_{i=1}^{n_t} \left(\mathbf{z}_i - \hat{\boldsymbol{\mu}}_{\mathbf{z}}^{(t+1)} \right)^T \left(\mathbf{z}_i - \hat{\boldsymbol{\mu}}_{\mathbf{z}}^{(t+1)} \right) \\
&= \sum_{i=1}^{n_t} \left(\mathbf{z}_i - \hat{\boldsymbol{\mu}}_{\mathbf{z}}^{(t)} + \hat{\boldsymbol{\mu}}_{\mathbf{z}}^{(t)} - \hat{\boldsymbol{\mu}}_{\mathbf{z}}^{(t+1)} \right)^T \left(\mathbf{z}_i - \hat{\boldsymbol{\mu}}_{\mathbf{z}}^{(t)} + \hat{\boldsymbol{\mu}}_{\mathbf{z}}^{(t)} - \hat{\boldsymbol{\mu}}_{\mathbf{z}}^{(t+1)} \right) \\
&= \sum_{i=1}^{n_t} \left(\mathbf{z}_i - \hat{\boldsymbol{\mu}}_{\mathbf{z}}^{(t)} \right)^T \left(\mathbf{z}_i - \hat{\boldsymbol{\mu}}_{\mathbf{z}}^{(t)} \right) + \sum_{i=1}^{n_t} \left(\hat{\boldsymbol{\mu}}_{\mathbf{z}}^{(t)} - \hat{\boldsymbol{\mu}}_{\mathbf{z}}^{(t+1)} \right)^T \left(\hat{\boldsymbol{\mu}}_{\mathbf{z}}^{(t)} - \hat{\boldsymbol{\mu}}_{\mathbf{z}}^{(t+1)} \right) \\
&+ \sum_{i=1}^{n_t} \left(\mathbf{z}_i - \hat{\boldsymbol{\mu}}_{\mathbf{z}}^{(t)} \right)^T \left(\hat{\boldsymbol{\mu}}_{\mathbf{z}}^{(t)} - \hat{\boldsymbol{\mu}}_{\mathbf{z}}^{(t+1)} \right) \sum_{i=1}^{n_t} \left(\hat{\boldsymbol{\mu}}_{\mathbf{z}}^{(t)} - \hat{\boldsymbol{\mu}}_{\mathbf{z}}^{(t+1)} \right)^T \left(\mathbf{z}_i - \hat{\boldsymbol{\mu}}_{\mathbf{z}}^{(t)} \right)
\end{aligned}$$

By calculation, we see

$$\begin{aligned}
\sum_{i=1}^{n_t} \left(\mathbf{z}_i - \hat{\boldsymbol{\mu}}_{\mathbf{z}}^{(t)} \right)^T \left(\hat{\boldsymbol{\mu}}_{\mathbf{z}}^{(t)} - \hat{\boldsymbol{\mu}}_{\mathbf{z}}^{(t+1)} \right) &= \left[\sum_{i=1}^{n_t} \left(\mathbf{z}_i - \hat{\boldsymbol{\mu}}_{\mathbf{z}}^{(t)} \right)^T \right] \left(\hat{\boldsymbol{\mu}}_{\mathbf{z}}^{(t)} - \hat{\boldsymbol{\mu}}_{\mathbf{z}}^{(t+1)} \right) \\
&= \left[\sum_{i=1}^{n_t} \mathbf{z}_i - \hat{\boldsymbol{\mu}}_{\mathbf{z}}^{(t)} \right]^T \left(\hat{\boldsymbol{\mu}}_{\mathbf{z}}^{(t)} - \hat{\boldsymbol{\mu}}_{\mathbf{z}}^{(t+1)} \right) \\
&= \left[\sum_{i=1}^{n_t} \mathbf{z}_i - \sum_{i=1}^{n_t} \hat{\boldsymbol{\mu}}_{\mathbf{z}}^{(t)} \right]^T \left(\hat{\boldsymbol{\mu}}_{\mathbf{z}}^{(t)} - \hat{\boldsymbol{\mu}}_{\mathbf{z}}^{(t+1)} \right) \\
&= [n_t \hat{\boldsymbol{\mu}}_{\mathbf{z}}^{(t)} - n_t \hat{\boldsymbol{\mu}}_{\mathbf{z}}^{(t)}]^T \left(\hat{\boldsymbol{\mu}}_{\mathbf{z}}^{(t)} - \hat{\boldsymbol{\mu}}_{\mathbf{z}}^{(t+1)} \right) \\
&= \mathbf{0}
\end{aligned}$$

Similarly,

$$\sum_{i=1}^{n_t} \left(\hat{\boldsymbol{\mu}}_{\mathbf{z}}^{(t)} - \hat{\boldsymbol{\mu}}_{\mathbf{z}}^{(t+1)} \right)^T \left(\mathbf{z}_i - \hat{\boldsymbol{\mu}}_{\mathbf{z}}^{(t)} \right) = \mathbf{0}.$$

Thus,

$$\begin{aligned}
& \sum_{i=1}^{n_t} \left(\mathbf{z}_i - \hat{\boldsymbol{\mu}}_{\mathbf{z}}^{(t+1)} \right)^T \left(\mathbf{z}_i - \hat{\boldsymbol{\mu}}_{\mathbf{z}}^{(t+1)} \right) \\
&= n_t \hat{\boldsymbol{\Sigma}}_{\mathbf{z}}^{(t)} + \sum_{i=1}^{n_t} \left(\hat{\boldsymbol{\mu}}_{\mathbf{z}}^{(t)} - \hat{\boldsymbol{\mu}}_{\mathbf{z}}^{(t+1)} \right)^T \left(\hat{\boldsymbol{\mu}}_{\mathbf{z}}^{(t)} - \hat{\boldsymbol{\mu}}_{\mathbf{z}}^{(t+1)} \right) \\
&= n_t \hat{\boldsymbol{\Sigma}}_{\mathbf{z}}^{(t)} + n_t \left(\hat{\boldsymbol{\mu}}_{\mathbf{z}}^{(t)} - \hat{\boldsymbol{\mu}}_{\mathbf{z}}^{(t+1)} \right)^T \left(\hat{\boldsymbol{\mu}}_{\mathbf{z}}^{(t)} - \hat{\boldsymbol{\mu}}_{\mathbf{z}}^{(t+1)} \right) \\
&= n_t \hat{\boldsymbol{\Sigma}}_{\mathbf{z}}^{(t)} + n_t \left(\hat{\boldsymbol{\mu}}_{\mathbf{z}}^{(t)} - \frac{n_t \hat{\boldsymbol{\mu}}_{\mathbf{z}}^{(t)} + n_b \hat{\boldsymbol{\mu}}_{\mathbf{z}}^{(b)}}{n_t + n_b} \right)^T \left(\hat{\boldsymbol{\mu}}_{\mathbf{z}}^{(t)} - \frac{n_t \hat{\boldsymbol{\mu}}_{\mathbf{z}}^{(t)} + n_b \hat{\boldsymbol{\mu}}_{\mathbf{z}}^{(b)}}{n_t + n_b} \right) \\
&= n_t \hat{\boldsymbol{\Sigma}}_{\mathbf{z}}^{(t)} + \frac{n_t n_b^2}{(n_t + n_b)^2} \left(\hat{\boldsymbol{\mu}}_{\mathbf{z}}^{(t)} - \hat{\boldsymbol{\mu}}_{\mathbf{z}}^{(b)} \right)^T \left(\hat{\boldsymbol{\mu}}_{\mathbf{z}}^{(t)} - \hat{\boldsymbol{\mu}}_{\mathbf{z}}^{(b)} \right)
\end{aligned}$$

Applying the same techniques to the second sum term, we obtain

$$\begin{aligned}
& \sum_{i=n_t+1}^{n_t+n_b} \left(\mathbf{z}_i - \hat{\boldsymbol{\mu}}_{\mathbf{z}}^{(t+1)} \right)^T \left(\mathbf{z}_i - \hat{\boldsymbol{\mu}}_{\mathbf{z}}^{(t+1)} \right) \\
&= \sum_{i=n_t+1}^{n_t+n_b} \left(\mathbf{z}_i - \hat{\boldsymbol{\mu}}_{\mathbf{z}}^{(b)} + \hat{\boldsymbol{\mu}}_{\mathbf{z}}^{(b)} - \hat{\boldsymbol{\mu}}_{\mathbf{z}}^{(t+1)} \right)^T \left(\mathbf{z}_i - \hat{\boldsymbol{\mu}}_{\mathbf{z}}^{(b)} + \hat{\boldsymbol{\mu}}_{\mathbf{z}}^{(b)} - \hat{\boldsymbol{\mu}}_{\mathbf{z}}^{(t+1)} \right) \\
&= \sum_{i=n_t+1}^{n_t+n_b} \left(\mathbf{z}_i - \hat{\boldsymbol{\mu}}_{\mathbf{z}}^{(b)} \right)^T \left(\mathbf{z}_i - \hat{\boldsymbol{\mu}}_{\mathbf{z}}^{(b)} \right) + \sum_{i=n_t+1}^{n_t+n_b} \left(\hat{\boldsymbol{\mu}}_{\mathbf{z}}^{(b)} - \hat{\boldsymbol{\mu}}_{\mathbf{z}}^{(t+1)} \right)^T \left(\hat{\boldsymbol{\mu}}_{\mathbf{z}}^{(b)} - \hat{\boldsymbol{\mu}}_{\mathbf{z}}^{(t+1)} \right) \\
&\quad + \sum_{i=n_t+1}^{n_t+n_b} \left(\mathbf{z}_i - \hat{\boldsymbol{\mu}}_{\mathbf{z}}^{(b)} \right)^T \left(\hat{\boldsymbol{\mu}}_{\mathbf{z}}^{(t)} - \hat{\boldsymbol{\mu}}_{\mathbf{z}}^{(t+1)} \right) + \sum_{i=n_t+1}^{n_t+n_b} \left(\hat{\boldsymbol{\mu}}_{\mathbf{z}}^{(b)} - \hat{\boldsymbol{\mu}}_{\mathbf{z}}^{(t+1)} \right)^T \left(\mathbf{z}_i - \hat{\boldsymbol{\mu}}_{\mathbf{z}}^{(t)} \right) \\
&= \sum_{i=n_t+1}^{n_t+n_b} \left(\mathbf{z}_i - \hat{\boldsymbol{\mu}}_{\mathbf{z}}^{(b)} \right)^T \left(\mathbf{z}_i - \hat{\boldsymbol{\mu}}_{\mathbf{z}}^{(b)} \right) + \sum_{i=n_t+1}^{n_t+n_b} \left(\hat{\boldsymbol{\mu}}_{\mathbf{z}}^{(b)} - \hat{\boldsymbol{\mu}}_{\mathbf{z}}^{(t+1)} \right)^T \left(\hat{\boldsymbol{\mu}}_{\mathbf{z}}^{(b)} - \hat{\boldsymbol{\mu}}_{\mathbf{z}}^{(t+1)} \right) \\
&= n_b \hat{\boldsymbol{\Sigma}}_{\mathbf{z}}^{(b)} + n_b \left(\hat{\boldsymbol{\mu}}_{\mathbf{z}}^{(b)} - \hat{\boldsymbol{\mu}}_{\mathbf{z}}^{(t+1)} \right)^T \left(\hat{\boldsymbol{\mu}}_{\mathbf{z}}^{(b)} - \hat{\boldsymbol{\mu}}_{\mathbf{z}}^{(t+1)} \right) \\
&= n_b \hat{\boldsymbol{\Sigma}}_{\mathbf{z}}^{(b)} + n_b \left(\hat{\boldsymbol{\mu}}_{\mathbf{z}}^{(b)} - \frac{n_t \hat{\boldsymbol{\mu}}_{\mathbf{z}}^{(t)} + n_b \hat{\boldsymbol{\mu}}_{\mathbf{z}}^{(b)}}{n_t + n_b} \right)^T \left(\hat{\boldsymbol{\mu}}_{\mathbf{z}}^{(b)} - \frac{n_t \hat{\boldsymbol{\mu}}_{\mathbf{z}}^{(t)} + n_b \hat{\boldsymbol{\mu}}_{\mathbf{z}}^{(b)}}{n_t + n_b} \right) \\
&= n_b \hat{\boldsymbol{\Sigma}}_{\mathbf{z}}^{(b)} + \frac{n_t^2 n_b}{(n_t + n_b)^2} \left(\hat{\boldsymbol{\mu}}_{\mathbf{z}}^{(b)} - \hat{\boldsymbol{\mu}}_{\mathbf{z}}^{(t)} \right)^T \left(\hat{\boldsymbol{\mu}}_{\mathbf{z}}^{(b)} - \hat{\boldsymbol{\mu}}_{\mathbf{z}}^{(t)} \right)
\end{aligned}$$

Therefore,

$$\begin{aligned}
\hat{\boldsymbol{\Sigma}}_{\mathbf{z}}^{(t+1)} &= \frac{1}{n_t + n_b} \left[n_t \hat{\boldsymbol{\Sigma}}_{\mathbf{z}}^{(t)} + \frac{n_t n_b^2}{(n_t + n_b)^2} \left(\hat{\boldsymbol{\mu}}_{\mathbf{z}}^{(t)} - \hat{\boldsymbol{\mu}}_{\mathbf{z}}^{(b)} \right)^T \left(\hat{\boldsymbol{\mu}}_{\mathbf{z}}^{(t)} - \hat{\boldsymbol{\mu}}_{\mathbf{z}}^{(b)} \right) + n_b \hat{\boldsymbol{\Sigma}}_{\mathbf{z}}^{(b)} \right. \\
&\quad \left. + \frac{n_t^2 n_b}{(n_t + n_b)^2} \left(\hat{\boldsymbol{\mu}}_{\mathbf{z}}^{(b)} - \hat{\boldsymbol{\mu}}_{\mathbf{z}}^{(t)} \right)^T \left(\hat{\boldsymbol{\mu}}_{\mathbf{z}}^{(b)} - \hat{\boldsymbol{\mu}}_{\mathbf{z}}^{(t)} \right) \right] \\
&= \frac{n_t}{n_t + n_b} \hat{\boldsymbol{\Sigma}}_{\mathbf{z}}^{(t)} + \frac{n_b}{n_t + n_b} \hat{\boldsymbol{\Sigma}}_{\mathbf{z}}^{(b)} + \frac{n_t n_b}{(n_t + n_b)^2} \left(\hat{\boldsymbol{\mu}}_{\mathbf{z}}^{(t)} - \hat{\boldsymbol{\mu}}_{\mathbf{z}}^{(b)} \right)^T \left(\hat{\boldsymbol{\mu}}_{\mathbf{z}}^{(t)} - \hat{\boldsymbol{\mu}}_{\mathbf{z}}^{(b)} \right) \quad (14)
\end{aligned}$$

C Mode

Note that the mean, variance, and mode of a log normal distribution with logarithm of location μ and logarithm of scale σ are given by the following formulas:

$$\mu_z = e^{\mu + \frac{1}{2}\sigma^2}, \sigma_z^2 = \left(e^{\sigma^2} - 1 \right) e^{2\mu + \sigma^2}, m_z = e^{\mu - \sigma^2}$$

Then the mode m_z can be expressed by the mean and variance,

$$m_z = e^{\mu + \frac{1}{2}\sigma^2 - \frac{3}{2}\sigma^2} = \underbrace{e^{\mu + \frac{1}{2}\sigma^2}}_{\mu_z} e^{-\frac{3}{2}\sigma^2} = \mu_z \left(\frac{\sigma_z^2}{\mu_z^2} + 1 \right)^{-\frac{3}{2}}$$

as

$$\begin{aligned}
\frac{\sigma_z^2}{\mu_z^2} &= \frac{\left(e^{\sigma^2} - 1 \right) e^{2\mu + \sigma^2}}{\left(e^{\mu + \frac{1}{2}\sigma^2} \right)^2} = \frac{\left(e^{\sigma^2} - 1 \right) e^{2\mu + \sigma^2}}{e^{2\mu + \sigma^2}} = e^{\sigma^2} - 1 \\
\Rightarrow e^{\sigma^2} &= \frac{\sigma_z^2}{\mu_z^2} + 1 \Rightarrow e^{-\frac{3}{2}\sigma^2} = \left(\frac{\sigma_z^2}{\mu_z^2} + 1 \right)^{-\frac{3}{2}}
\end{aligned}$$

D Proof of Proposition

Note that the marginal distribution of the reconstruction feature under p_m is given by $\frac{1}{2}p_0(z) + \frac{1}{2}p_t(z)$, where p_0 denotes the marginal distribution of the reconstruction feature in the data distribution p_d . For any $z \in [0, m_z]$, we have

$$\begin{aligned}
\frac{1}{2}p_0(z) + \frac{1}{2}p_t(z) &= \frac{1}{2}p_0(z) + \frac{1}{2} \cdot \frac{\frac{1}{\sqrt{2\pi\sigma_z^2}} e^{-\frac{(z-m_z)^2}{2\sigma_z^2}}}{\Phi(\frac{m_z-m_z}{\sigma_z}) - \Phi(\frac{0-m_z}{\sigma_z})} \\
&= \frac{1}{2}p_0(z) + \frac{1}{2} \cdot \frac{\frac{1}{\sqrt{2\pi\sigma_z^2}} e^{-\frac{(z-m_z)^2}{2\sigma_z^2}}}{\frac{1}{2} - \Phi(\frac{0-m_z}{\sigma_z})} \\
&\geq \frac{1}{2}p_0(z) + \frac{1}{2} \cdot \frac{\frac{1}{\sqrt{2\pi\sigma_z^2}} e^{-\frac{(z-m_z)^2}{2\sigma_z^2}}}{\frac{1}{2}} \\
&= \frac{1}{2}p_0(z) + \frac{1}{\sqrt{2\pi\sigma_z^2}} e^{-\frac{(z-m_z)^2}{2\sigma_z^2}} \\
&\geq \frac{1}{2}p_0(z) + \frac{1}{\sqrt{2\pi\sigma_z^2}} e^{-\frac{(z-\mu_z)^2}{2\sigma_z^2}} \\
&\geq \frac{1}{\sqrt{2\pi\sigma_z^2}} e^{-\frac{(z-\mu_z)^2}{2\sigma_z^2}} \\
&= p_n(z)
\end{aligned}$$

where the second inequality is according to the fact $m_z \leq \mu_z$.

E Experimental Setup

All experiments are conducted on an HP Z4 G4 Workstation equipped with an NVIDIA RTX 3090 GPU (24 GB VRAM). The software environment is set up using a Conda virtual environment with PyTorch 2.4.1 and Scikit-Learn 1.5.1. Unless otherwise stated, each experiment is repeated five times to assess performance stability. Additionally, the noise-sample ratio ν is fixed at 8 unless specified otherwise. To prevent overfitting during AE and NCE training, we reserve 20% of the training data as a validation set for model selection, choosing the model that achieves the lowest validation loss. Note that both the training and validation sets consist solely of normal samples.

For the evaluation of DAGMM on MNIST and CIFAR-10, and DROCC on MNIST-C, we use the authors' publicly available code, with minor modifications as described in the corresponding sections. Refer to those sections for further details.

F Ablation

In addition to the overall performance shown averaged across all 10 classes in Table 1, Table 7 provides a class-wise results on MNIST and CIFAR-10. LatNCE and CNCE have similar performance on CIFAR-10 dataset, but CNCE has significantly higher performance across the 10 classes at a significance threshold of 0.01 for a one-sided Wilcoxon signed-rank test (p-value of 0.00488). CANCE is higher performance than CNCE on 17 of the 20 cases.

A similar ablation study is conducted on the multimodal training dataset, where different combinations of classes—specifically (0, 1), (0, 8), and (1, 8)—are treated as normal, while the remaining classes are considered anomalous. In all settings, CANCE consistently achieves the best or nearly best performance, demonstrating the effectiveness of its individual components.

For the ResNet-18 feature extraction shown in Table 9, CNCE consistently outperforms LatNCE, highlighting the effectiveness of including reconstruction error in density estimation. Additionally, augmenting indeed helps detect anomalies, as evidenced by the gap between CANCE and CNCE.

Table 7: Ablation study on unimodal training dataset

Data	Error	LatNCE	CNCE	CANCE
MNIST				
0	99.4 \pm 0.1	85.0 \pm 3.5	99.5 \pm 0.0	99.6 \pm 0.0
1	99.9 \pm 0.0	98.4 \pm 0.3	99.8 \pm 0.0	99.8 \pm 0.0
2	90.3 \pm 1.5	81.9 \pm 6.5	96.6 \pm 0.7	97.1 \pm 0.5
3	92.6 \pm 0.6	81.2 \pm 1.2	95.6 \pm 0.4	96.7 \pm 0.3
4	95.5 \pm 1.3	75.0 \pm 3.8	95.8 \pm 0.3	96.9 \pm 0.4
5	95.1 \pm 1.5	76.1 \pm 4.8	96.1 \pm 0.4	97.2 \pm 0.4
6	98.9 \pm 0.3	88.2 \pm 4.3	99.2 \pm 0.0	99.4 \pm 0.0
7	96.1 \pm 0.6	89.1 \pm 2.1	96.9 \pm 0.6	97.5 \pm 0.3
8	85.8 \pm 0.4	80.6 \pm 1.3	94.6 \pm 0.5	95.6 \pm 0.3
9	97.0 \pm 0.3	86.0 \pm 1.5	96.2 \pm 0.2	97.1 \pm 0.1
Avg	95.1	84.1	97.0	97.7
CIFAR-10				
0	57.8 \pm 2.3	63.4 \pm 2.0	63.4 \pm 2.3	63.8 \pm 2.3
1	33.8 \pm 1.5	63.4 \pm 1.2	63.4 \pm 0.7	63.6 \pm 0.8
2	65.0 \pm 0.4	59.5 \pm 1.8	59.9 \pm 1.8	60.0 \pm 1.7
3	54.6 \pm 0.5	62.3 \pm 1.9	62.2 \pm 2.0	62.3 \pm 2.1
4	71.0 \pm 0.8	68.9 \pm 1.6	69.3 \pm 1.7	69.4 \pm 1.5
5	54.6 \pm 0.8	61.1 \pm 1.1	61.5 \pm 1.2	61.6 \pm 1.1
6	55.2 \pm 2.9	73.0 \pm 2.4	73.0 \pm 2.4	73.0 \pm 2.3
7	44.7 \pm 0.7	61.1 \pm 1.1	61.3 \pm 1.1	61.2 \pm 1.0
8	67.8 \pm 0.8	71.9 \pm 2.1	72.4 \pm 2.1	72.3 \pm 2.3
9	36.4 \pm 1.1	66.3 \pm 1.6	66.9 \pm 1.7	66.5 \pm 1.5
Avg	54.1	65.1	65.3	65.4

Table 8: Ablation study on the multimodal datasets

Data	Error	LatNCE	CNCE	CANCE
MNIST				
0, 1	99.4 \pm 0.1	93.8 \pm 1.1	99.5 \pm 0.1	99.6 \pm 0.1
0, 8	87.8 \pm 0.7	79.8 \pm 1.3	95.0 \pm 0.5	95.5 \pm 0.4
1, 8	96.7 \pm 0.7	89.3 \pm 2.3	97.4 \pm 0.3	97.8 \pm 0.2
Avg	94.6	87.6	97.3	97.6
CIFAR-10				
0, 1	44.4 \pm 1.3	53.9 \pm 0.9	54.5 \pm 1.3	54.8 \pm 1.1
0, 8	65.7 \pm 1.7	64.4 \pm 5.2	64.6 \pm 5.7	64.7 \pm 5.7
1, 8	48.9 \pm 0.7	63.3 \pm 1.8	63.4 \pm 1.7	63.1 \pm 1.5
Avg	53.0	60.5	60.8	60.9

However, unlike in Table 7, LatNCE and CNCE are not competitive with Error on average. There are two potential reasons for this: first, the latent feature extracted by PCA is simple and thus less useful compared to AE; second, the density estimator induced by NCE does not capture data distribution well enough for anomaly detection. However, CANCE outperforms Error, meaning there is still information in the latent representation.

G Detailed Results

As extensions of Tables 2 and 4, Tables 10 and 11 present detailed class-wise comparative results.

In Table 10, the AEs compress images from MNIST and CIFAR-10 to dimensions 6 and 64, respectively, with regularization coefficients λ (see Appendix A) set to 0.3 and 0.004, respectively. In Table 11, PCA is applied to features extracted by ResNet-18, reducing them to the same dimensions—6 for MNIST and 64 for CIFAR-10.

H DAGMM

We conduct an extra comparison between CANCE and DAGMM Zong et al. [2018] since both methods employ latent and reconstruction feature for anomaly detection. In this experiment, we

Table 9: Ablation study on features extracted by ResNet-18 on MNIST and CIFAR-10

Data	Error	LatNCE	CNCE	CANCE
MNIST				
0	98.1 \pm 0.0	78.4 \pm 0.9	96.7 \pm 0.6	98.6 \pm 0.0
1	99.8 \pm 0.0	98.6 \pm 0.1	99.6 \pm 0.0	99.7 \pm 0.0
2	88.3 \pm 0.0	74.4 \pm 0.7	83.8 \pm 1.4	91.0 \pm 0.1
3	95.1 \pm 0.0	74.1 \pm 0.5	92.5 \pm 0.3	94.7 \pm 0.2
4	97.3 \pm 0.0	84.4 \pm 0.5	96.3 \pm 0.3	97.3 \pm 0.2
5	92.2 \pm 0.0	60.8 \pm 0.2	87.7 \pm 0.5	91.5 \pm 0.4
6	94.8 \pm 0.0	72.7 \pm 0.8	93.5 \pm 0.2	94.6 \pm 0.2
7	96.8 \pm 0.0	85.5 \pm 1.2	96.3 \pm 0.3	96.8 \pm 0.3
8	91.0 \pm 0.0	75.4 \pm 1.1	85.8 \pm 1.5	92.1 \pm 0.5
9	92.0 \pm 0.0	65.5 \pm 0.6	89.1 \pm 0.4	93.3 \pm 0.2
Avg	94.5	77.0	92	95.0
CIFAR-10				
0	88.5 \pm 0.1	75.5 \pm 0.8	80.9 \pm 1.6	86.5 \pm 0.4
1	94.6 \pm 0.0	90.9 \pm 0.3	93.5 \pm 0.6	95.3 \pm 0.1
2	77.0 \pm 0.1	60.0 \pm 0.2	63.9 \pm 3.1	75.1 \pm 0.3
3	80.3 \pm 0.1	71.3 \pm 1.6	75.1 \pm 1.7	78.8 \pm 0.7
4	90.2 \pm 0.0	81.2 \pm 0.8	85.8 \pm 1.0	89.2 \pm 0.3
5	84.1 \pm 0.0	68.6 \pm 1.2	76.9 \pm 2.7	87.0 \pm 0.4
6	90.4 \pm 0.1	80.5 \pm 0.7	85.7 \pm 0.9	88.9 \pm 0.9
7	86.5 \pm 0.1	76.0 \pm 0.5	85.4 \pm 2.7	91.1 \pm 0.4
8	91.7 \pm 0.1	83.1 \pm 0.6	88.7 \pm 0.3	92.4 \pm 0.3
9	94.6 \pm 0.0	88.7 \pm 0.9	93.4 \pm 0.8	95.8 \pm 0.1
Avg	87.8	77.6	82.9	88.0

use the same neural networks and training strategy as in DAGMM except three modifications: 1) DAGMM is only trained over 10 epochs instead of 200 epochs; 2) the reconstruction error is $\frac{\|\mathbf{x} - \mathbf{x}'\|^2}{d_0}$ rather than the relative Euclidean distance $\frac{\|\mathbf{x} - \mathbf{x}'\|}{\|\mathbf{x}\|}$; and the cosine dissimilarity $\frac{1}{2} \left(1 - \frac{\mathbf{x}^T \mathbf{x}'}{\|\mathbf{x}\| \|\mathbf{x}'\|}\right)$ is utilized rather than the cosine similarity $\frac{\mathbf{x}^T \mathbf{x}'}{\|\mathbf{x}\| \|\mathbf{x}'\|}$. We observe that the training loss of DAGMM converges in less than 10 epochs, making it unnecessary to train the model for 200 epochs. Since the reconstruction error is used as an anomaly score instead of the relative Euclidean distance in AE, it is more reasonable to include the reconstruction error as a component of the composite feature. The reconstruction error is scaled by the data dimension d_0 to ensure its value remains small. Additionally, we choose cosine dissimilarity over cosine similarity because it is non-negative, similar to the reconstruction error.

We independently run the experiment 20 times on the dataset KDDCUP99⁴, as done in DAGMM, and summarize the average precision, recall, and F_1 score in Table 12. The values for DAGMM-0 are extracted from Table 2 in the DAGMM paper. The results for DAGMM-1 were obtained by training DAGMM with three modifications as mentioned earlier. The last row, DAGMM-CANCE, involves training a DAGMM first for feature learning and then using our method, CANCE, for density estimation. Clearly, DAGMM-1 achieves better performance than DAGMM-0. Furthermore, DAGMM-CANCE achieves comparable results to DAGMM-1. We argue that separately optimizing the compression network and estimation network will not degrade the method’s performance, provided they are well designed and optimized.

I DPAD

CANCE is also evaluated on the Fashion-MNIST dataset, using the same neural network architecture and hyperparameters as in the MNIST experiments. While its performance is slightly lower than that of DPAD, it still outperforms all other baselines. With appropriate adjustments to the network architecture and hyperparameters, CANCE is expected to achieve comparable or even better performance.

⁴Refer to the DAGMM paper for the implementation details.

Table 10: AUCROC [%] for baseline methods, Pix-CNN (PC) and DAGMM, compared to CANCE mean and std. value across 5 independent runs.

Data	KDE	VAE	PC	LSA	DAGMM	CANCE
MNIST						
0	88.5	99.8	53.1	99.3	53.6	99.6 ± 0.0
1	99.6	99.9	99.5	99.9	51.5	99.8 ± 0.0
2	71.0	96.2	47.6	95.9	53.5	97.1 ± 0.5
3	69.3	94.7	51.7	96.6	49.7	96.7 ± 0.3
4	84.4	96.5	73.9	95.6	52.7	96.9 ± 0.4
5	77.6	96.3	54.2	96.4	54.3	97.2 ± 0.4
6	86.1	99.5	59.2	99.4	55.2	99.4 ± 0.0
7	88.4	97.4	78.9	98.0	53.8	97.5 ± 0.3
8	66.9	90.5	34.0	95.3	54.8	95.6 ± 0.3
9	82.5	97.8	66.2	98.1	51.8	97.1 ± 0.1
Avg	81.4	96.9	61.8	97.5	53.1	97.7
CIFAR-10						
0	65.8	68.8	78.8	73.5	47.5	63.8 ± 2.3
1	52.0	40.3	42.8	58.0	47.2	63.6 ± 0.8
2	65.7	67.9	61.7	69.0	46.1	60.0 ± 1.7
3	49.7	52.8	57.4	54.2	47.3	62.3 ± 2.1
4	72.7	74.8	51.1	76.1	48.5	69.4 ± 1.5
5	49.6	51.9	57.1	54.6	48.9	61.6 ± 1.1
6	75.8	69.5	42.2	75.1	47.8	73.0 ± 2.3
7	56.4	50.0	45.4	53.5	47.6	61.2 ± 1.0
8	68.0	70.0	71.5	71.7	48.4	72.3 ± 2.3
9	54.0	39.8	42.6	54.8	48.1	66.5 ± 1.5
Avg	61.0	58.6	55.1	64.1	47.7	65.4

Table 11: AUROC[%] on CIFAR-10 for baseline methods. Nearest neighbor (NN) baseline uses either original space or like CANCE the ResNet-18 features.

Data	DSVDD	NN	DROCC	DPAD	CANCE
0	61.7 ± 4.1	69.0	80.0	81.7 ± 0.2	78.0 ± 0.3
1	65.9 ± 2.1	44.2	90.5	76.7 ± 1.0	75.0 ± 0.2
2	50.8 ± 0.8	68.3	64.7	66.7 ± 1.0	68.1 ± 0.5
3	59.1 ± 1.4	51.3	71.5	67.1 ± 1.5	66.7 ± 0.4
4	60.9 ± 1.1	76.7	83.8	73.6 ± 2.0	77.9 ± 0.8
5	65.7 ± 2.5	50.0	70.0	74.4 ± 2.0	68.6 ± 0.3
6	67.7 ± 2.6	72.4	83.0	74.4 ± 0.9	81.2 ± 0.4
7	67.3 ± 0.9	51.3	76.7	74.3 ± 0.2	74.8 ± 0.2
8	75.9 ± 1.2	69.0	82.8	80.0 ± 1.7	79.1 ± 1.0
9	73.1 ± 1.2	43.3	87.5	76.2 ± 0.7	76.1 ± 0.2
Avg	64.8	59.5	79.1	74.2	74.5
					88.0

Table 12: Anomaly detection results on contaminated training data from KDDCUP99

Method	Precision	Recall	F_1
DAGMM-0	93.0	94.4	93.7
DAGMM-1	97.7 ± 0.3	96.9 ± 0.6	97.3 ± 0.5
DAGMM-CANCE	97.6 ± 0.3	96.9 ± 0.6	97.3 ± 0.5

Table 13: AUROC[%] CANCE vs DPAD on F-MNIST.

Data	DAGMM	DSVDD	DROCC	DPAD	CANCE
0	42.1	79.1	88.1	93.7 ± 0.2	90.6 ± 0.4
1	55.1	94.0	97.7	98.7 ± 0.0	98.4 ± 0.1
2	50.4	83.0	87.6	90.3 ± 0.0	89.0 ± 0.4
3	57.0	82.9	87.7	94.7 ± 0.3	91.8 ± 0.6
4	26.9	87.0	87.2	92.2 ± 0.1	90.7 ± 0.2
5	70.5	80.3	91.0	93.9 ± 0.8	92.6 ± 1.0
6	48.3	74.9	77.1	82.3 ± 0.1	83.5 ± 0.2
7	83.5	94.2	95.3	98.7 ± 0.1	97.8 ± 0.2
8	49.9	79.1	82.7	94.2 ± 0.6	91.7 ± 1.1
9	34.0	93.2	95.9	98.1 ± 0.2	98.3 ± 0.1
Avg	51.7	84.7	89.0	93.7	92.5